Physica Scripta

PAPER

Transport characteristics and lattice dynamics with phonon topology accentuation in layered CuTlX (X: S, Se)

To cite this article: Sushree Sarita Sahoo and V Kanchana 2022 *Phys. Scr.* **97** 125820

IOP Publishing   *Phys. Scr.* **97** (2022) 125820   https://doi.org/10.1088/1402-4896/aca059

Physica Scripta

RECEIVED
1 August 2022

REVISED
14 October 2022

ACCEPTED FOR PUBLICATION
4 November 2022

PUBLISHED
15 November 2022

PAPER

Transport characteristics and lattice dynamics with phonon topology accentuation in layered CuTlX (X: S, Se)

Sushree Sarita Sahoo and V Kanchana

Department of Physics, Indian Institute of Technology Hyderabad, Kandi 502285, Sangareddy, Telangana, India

E-mail: kanchana@iith.ac.in

Keywords: thermal conductivity, phonon topology, thermoelectric figure of merit, monolayer studies

Abstract

In recent years, numerous Cu-based compounds have attracted a great deal of interest for enhanced thermoelectric energy conversion. Here, we demonstrate that CuTlX (X: S, Se), a layered semiconductor, exhibits low lattice thermal conductivity (κ_l) and a high thermoelectric figure of merit (ZT), using density functional theory calculations and Boltzmann transport theory beyond relaxation time approximation. To evaluate the absolute values of thermoelectric coefficients, different scattering mechanisms such as acoustic deformation potential scattering, impurity phonon scattering, and polar optical phonon scattering are analysed. This low lattice thermal conductivity, which is complemented by a low group velocity and a low phonon lifetime, accounts for the remarkable thermoelectric efficiency in these compounds. In CuTlS, the contribution of the in-plane optical phonon mode to κ_l results in a decrease in its value, which might be attributed to the occurrence of Dirac-like crossings with non-trivial topological characteristics, as corroborated by the non-zero Berry curvature value. Overall, the thermoelectric behavior of both compounds is favorable at ambient temperature. Specifically, the out-of-plane direction in CuTlSe presents elevated thermoelectric performance with a high value for the thermoelectric figure of merit, with 1.08 and 1.16 for holes and electrons, respectively, at 300 K at the optimal carrier density of 10^{19} cm^{-3}, which well aids in both the electron and phonon transport. We also undertook monolayer examinations of these compounds due to the existence of van der Waals interactions, which predicted strong thermoelectric performance for both carrier concentrations at 300 K. As a result, our study presents a theoretical prediction on transport phenomena that requires experimental verification and should motivate additional research into prospective thermoelectric materials in the same crystal family for device applications.

1. Introduction

The escalating energy crisis, limited resources of fossil fuels and threatening global warming have made renewable, clean energy sources the elixir of the current world. Nowadays, power accessibility is a critical need for each society trying to flourish, leading to a never-ending growth of energy consumption. Because of this, a new era of sustainable energy will soon dawn as many benefits of renewable energy sources begin to surpass the current requirement. Therefore, the current challenge is creating sufficient power to satisfy rising energy demand by researching effective techniques of energy harvesting and optimising energy use while minimising environmental impact. In traditional energy sources, waste heat accounts for more than 60% of energy loss to the environment [1, 2]. As a result, high-performance thermoelectric (TE) materials have piqued attention owing to their ability to convert heat energy directly into electrical energy and vice versa, which can potentially be employed to address these obstacles [3, 4]. The interdepedency of TE parameters put forward substantial hurdles in enhancing the TE performance of materials. In TE devices, the Seebeck effect transforms heat into electricity, and the Peltier effect transforms electricity into heat. The low conversion efficiency and exorbitant prices of TE devices have hampered its widespread adoption, restricting its market development in the fields of electricity generation, heating, cooling, and waste heat recovery. The fundamental measure of material performance is the figure of merit, or *ZT*. Optimizing the unfavourably interrelated Seebeck coefficient, electrical conductivity and thermal conductivity as a group is crucial to maximize the *ZT*. Researchers have been searching for prospective TE materials for decades, developing numerous methods and unique ideas such as coherent phonons, topological electrons and phonons, rattling effects, non-phononic metamaterials, and so on [5–9]. The pursuit of high-performance TE materials has sparked broad interest in recent years, as seen by the remarkable growth in research into several classes of materials such as Pb (S, Se and Te), SnSe, SiGe alloys, (Bi, Sb)$_2$(Te, Se)$_3$, clathrates, skutterudites, half-Heusler alloys, and so on [10]. The present state-of-the-art thermoelectric materials are composed of expensive, toxic, rare or hazardous heavy elements like Pb, Te, Sb, Bi, Co, etc [11–15]. Cu-S and Cu-Se based compounds have been extensively studied for potential TE applications in the quest for a low-cost, environmentally innocuous, non-toxic, and naturally abundant material. Previous studies on Cu-S and Cu-Se based compounds showed the liquid-like behaviour of copper ions in these compounds led to very low lattice thermal conductivity (κ_l), which along with high electrical conductivity, resulting in a high *ZT* value i.e., Cu$_{2-x}$Se, reaches a *ZT* value of 1.5 at 1000 K, which is one of the highest for any bulk material [16–19]. CuTlX (X: S, Se) was chosen for further investigation because of this purpose. Layered ternary Copper thallium chalcogenides in single crystals CuTlX was synthesized by sandwiching CuX tetrahedra between Tl planes [20], which is structurally identical to LiFeAs superconductor [21]. A noteworthy aspect of a layered structure is that the intralayer and interlayer spacing may be adjusted independently, allowing for fine adjustment of the electrical and thermal transport properties. This is a favourable scenario for the development of high-performance thermoelectric materials.

The following is the layout of this paper: The details of the computation are discussed in section 2. In section 3, the mechanical and dynamical characteristics are examined (3.1). Section 3 (3.2 & 3.3) discuss the electronic and thermoelectric characteristics of bulk materials. Section 3.4 discusses monolayer studies. Section 4 provides the conclusion.

2. Computational details

The Vienna Ab-initio Simulation Package (VASP) code [22–25] algorithm, which uses the Generalized Gradient Approximation (GGA) [26] exchange and correlation functional, is used to execute the whole geometry optimization. We have combined the van der Waals (vdw) effect with the DFT-D3 approach [27] since this compound is layered. The plane-wave basis sets are created using a 10 × 10 × 5 k-mesh using Monkhorst-pack scheme [28]. The plane-wave expansion's cutoff energy is set at 900 eV. The tolerance values for energy and force convergence in structural optimization are 10^{-8} eV and 0.01 eV/Å, respectively. The Heyd-Scuseria-Ernzerhof (HSE06) [29] screened hybrid functional is used to provide a more precise understanding of the electronic structures and band gap. Phonon band spectrum is calculated using the combination of PHONOPY code [30] and density functional perturbation theory (DFPT) [31] as implemented in VASP. Effective phonon frequency was obtained to capture scattering from the full phonon band structure in a single phonon frequency which is a weighted sum over all Γ-point phonon modes. Topological nature of phonons were calculated using WANNIERTOOLS package [32]. κ_l calculations was performed on a supercell of 1 × 1 × 2 using phono3py package [33]. Thermoelectric properties and scattering rates are calculated using AMSET [34] code taking the inputs from wave function coefficients, elastic constants, deformation potentials, static and high-frequency dielectric constants, uniform band structure, and effective phonon frequency. Figure 1(a) displays the crystal structure of CuTlX, which belongs to tetragonal symmetry with nonsymmorphic space group *P4/nmm* (129). The irreducible Brillouin zone (IBZ) illustrating high symmetry points and the 001 plane is given in figure 1(b). The optimized parameters and experimental parameters are given in table 1.

3. Results and discussions

3.1. Mechanical and dynamical properties

The elastic constants (C$_{ij}$) of solids gives an idea about the inter-atomic interactions, mechanical stability, ductile or brittle nature and many other properties [35]. Elastic constants were determined by strain-stress relationships [36], as implemented in VASP software package and the same are tabulated in table 2. For tetragonal structure, a system must satisfy the given Born stability criteria [37]:

$$\begin{aligned}&C_{11} > 0, C_{33} > 0, C_{44} > 0, C_{66} > 0,\\&C_{11} - C_{12} > 0, C_{11} + C_{33} - 2C_{13} > 0,\\&2(C_{11} + C_{12}) + C_{13} + 4C_{13} > 0\end{aligned}$$

The calculated C$_{ij}$ satisfy all the stability criteria and further the bulk (B) and shear (G) moduli were estimated using the Voigt-Reuss-Hill technique [38–40]. In addition to B and G, the Young's modulus (E) and Poisson's

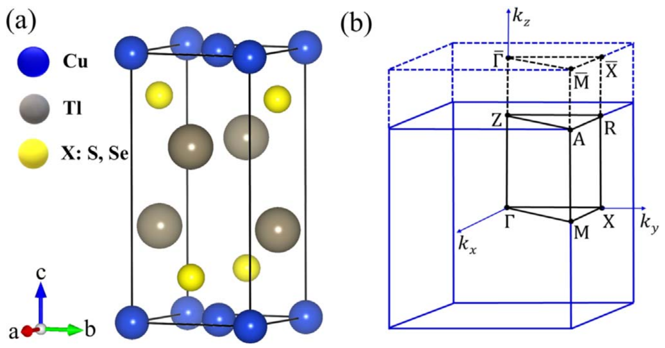

Figure 1. (a) Crystal structure of CuTlX, (b) The irreducible Brillouin zone.

Table 1. Optimized parameters of CuTlX (X = S, Se) and the experimental parameters.

Compounds	CuTlS			CuTlSe		
	a(Å)	c(Å)	V($Å^3$)	a(Å)	c(Å)	V($Å^3$)
Experimental [20]	3.92	8.12	124.95	4.09	8.20	136.89
GGA	3.94	8.52	132.66	4.13	8.40	143.59
DFT-D3	3.81	8.38	121.79	3.93	8.61	132.92

Table 2. Elastic constants of CuTlX, (X:S, Se).

Compound/Elastic constants	CuTlS	CuTlSe
C_{11} (GPa)	86.59	63.77
C_{12} (GPa)	39.30	21.68
C_{13} (GPa)	50.30	36.94
C_{33} (GPa)	53.48	42.10
C_{44} (GPa)	11.03	8.16
C_{66} (GPa)	12.35	8.60
Bulk Modulus (GPa)	55.10	40.70
Young's modulus (GPa)	31.62	24.08
Shear Modulus (GPa)	11.26	8.59
Poisson's ratio(ν)	0.404	0.401
Melting point (K)	693.98	608.46
Debye temperature(Θ_D)	145.07	119.54
Gr$u$neisen parameters(γ)	2.67	2.64

ratio (ν) have been calculated. The ductile or brittle nature of a material can also be determined from the Frantsevich's rule [41] which states that the material is ductile for a Poisson's ratio (ν) larger than 0.26. The present value of ν confirms the ductile nature of the compounds. Additionaly, we have calculated the Debye temperature (Θ_D) and Gr$\ddot{u}$neisen parameter (γ) for both the compounds [42]. A low value of Θ_D and high value of γ indicate the possibilities of low value of κ_l in these materials as most of the crystals have $1 < \gamma < 2$ [43]. We also used the relation given by Fine [44] to compute the melting temperatures for both compounds. For CuTlS, it is 694 K, while it is around 608 K for CuTlSe. We performed all subsequent computations at room temperature since the errors in this calculation are ±300 K. Table 2 summarises the mechanical properties measured.

Futher to examine the dynamical stability of these compounds, we have determined the phonon dispersion along the high-symmetry points, as shown in the IBZ figure 1(b). The phonon dispersion for both the compounds are shown in figure 2. We discovered that all phonon branches exist within the positive frequency domain demonstrating the dyanmical stability of the compounds. The maximum frequencies observed in CuTlS and CuTlSe are 8 THz and 5.2 THz, respectively, following the general pattern of decreasing phonon frequency with increasing atomic mass.

Phonon dispersion calculations from second-order harmonic interatomic force constants (IFCs) [33] can be used to determine the group velocities. Third-order anharmonic IFCs are being used to compute the three-phonon scattering rate, also known as the Umklapp process, which can be used to calculate the phonon lifetimes. Figure 3 illustrates that the group velocity is larger in the 'a' direction for both compounds than in the

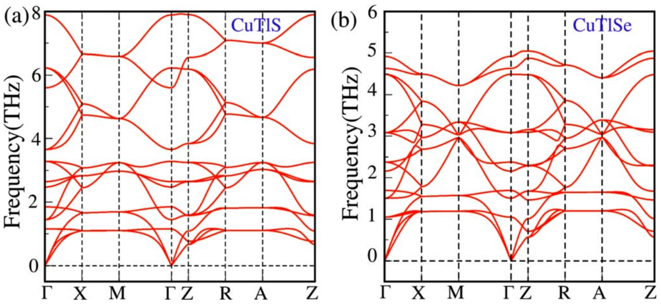

Figure 2. The calculated phonon spectrum, (a) CuTlS, (b) CuTlSe.

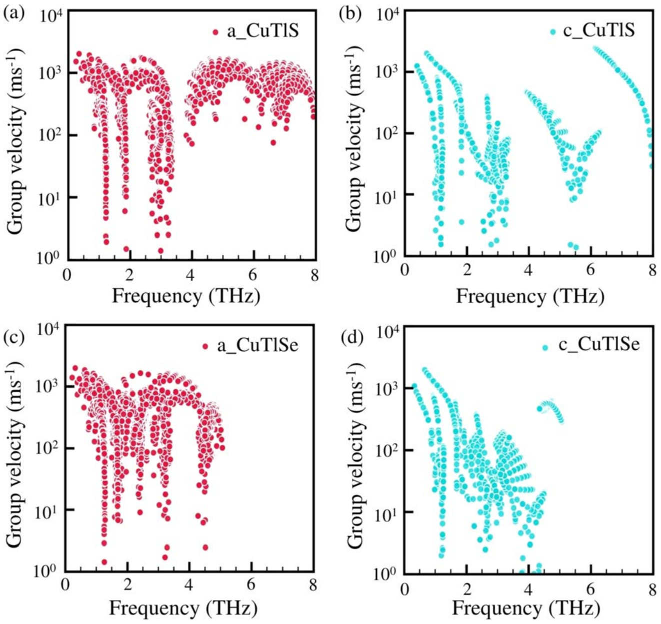

Figure 3. Group velocity of CuTlS (a) Along a-diretion (b) Along 'c' direction, of CuTlSe (c) Along 'a' direction (d) Along 'c' direction.

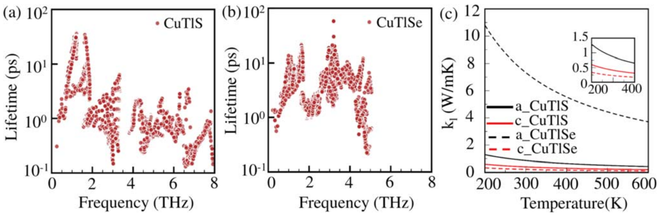

Figure 4. Phonon lifetime (a) CuTlS (b) CuTlSe (c) lattice thermal conductivity.

'c' direction due to the existence of out-of-plane weak vdw interaction. Furthermore, the phonon number density is higher along the 'a' direction when compared to the 'c' direction. We can see that the phonon number density is nearly identical across the entire phonon frequency range in the 'a' direction, implying that both acoustic and optical phonons contribute to phonon transport properties, while low frequency phonon modes contribute the most to the group velocity in the 'c' direction. Overall, the phonon number density of both compounds is comparable. The acoustic and optical modes are strongly coupled in CuTlSe, and the latter are projected to contribute very moderately to κ_l. CuTlSe has a shorter phonon lifetime than CuTlS in the acoustic area, indicating CuTlSe's ultra-low κ_l (figure 4(a), (b)). Figure 4(c) displays the estimated κ_l. As the temperature increases, the conductivity decreases. This is a typical behavior observed in the κ_l of crystalline materials, which results from the inherent amplification of phonon-phonon scattering as temperature increases. Based on the

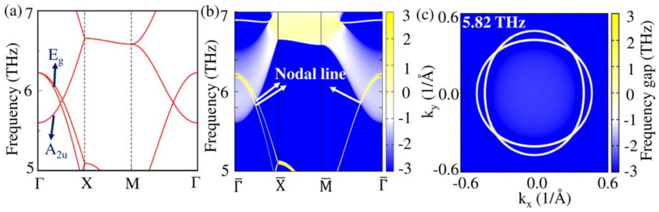

Figure 5. The 001 plane projected topological features of phonons CuTlS in 5-7 THz frequency. (a) Phonon spectra for inverted phonon bands, along with opposite mirror eigenvalues. (b) Bulk-crossings in phononic surface states projected in the 001 plane (highlighted with white arrows) (c) The nodal line that corresponds to these bulk band crossings (5.82 THz).

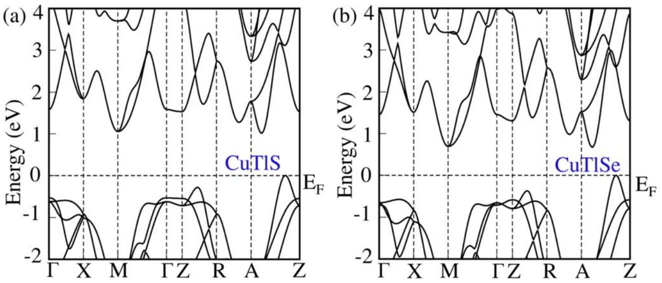

Figure 6. Band structure of (a) CuTlS, (b) CuTlSe.

calculated Debye temperature, Gr*ü*neisen parameters, group velocity, and phonon lifetime, CuTlSe should have lower κ_l than CuTlS, which contradicts our findings in 'a' direction (figure 4(c)). This discrepancy in the data piqued our interest, so we have analyzed the phonons of CuTlS in greater depth along the $\Gamma - X$ direction.

Using comprehensive phonon analysis, we discovered the Dirac-like crossing of phonon bands in the $\Gamma - X$ direction in optical modes between 5 and 6 THz. This intrigued us to study the topological nature of these Bosonic particles along this direction. Bosonic nature helped us to probe any frequency range to spot out topological nature. To begin, we performed a comprehensive mode analysis for this compound at the Gamma point. According to group theory, CuTlS has 18 modes, from which 3 are acoustic modes ($E_u + A_{2u}$), the rest are optic modes ($2E_u + 2A_{2u} + 3E_g + 2A_{1g} + B_{1g}$). Here E_u and E_g are doubly degenerate modes and rest are singly degenerate modes. Irreducible mode analysis confirm the optical-optical phonon mode inversion at the crossing point. The band 15 (singly degenerate A_{2u}) and 16 & 17 (doubly degenerate E_g) with opposite mirror eigen values form the crossing at 5.82 THz which is shown in the figure 5.

To further understand the topological character of the crossing point, we have used the Wannier90 programme to compute the tight-binding Hamiltonian and evaluated the surface states and iso-frequency spectrum in the 001 plane. Figure 5 depicts the corresponding surface states and nodal rings. Calculated Berry phase value furthermore confirms the presence of nontrivial topology. In centrosymmetric spinless systems with time-reversal symmetry [45], the nodal lines defined by the π Berry phase can emerge at general points in k space. This quantized value of the Berry phase surrounding the nodal lines makes them resistant to perturbations that break other space-group symmetries besides the inversion symmetry. A non-zero Berry phase value confirms the topological nature of those high frequency phonon states. Topologically protected states are immune to backscattering thus they suppress the κ_l in $\Gamma - X$ direction [46]. Consequently, when compared to CuTlSe, CuTlS has lower κ_l along the 'a' direction; nonetheless, in order to forecast the TE performance along this direction, power factor also plays a crucial role, which is discussed in the subsequent subsections.

3.2. Electronic structure properties and Scattering lifetime

The electronic band structures and density of states (DOS) of CuTlX are computed using HSE06 functionals to further investigate its electronic characteristics, as shown in figure 6. CuTlX has been discovered to be a narrow bandgap semiconductor according to prior theoretical studies, with bandgaps of 0.417 eV and 0.166 eV for CuTlS and CuTlSe, respectively [20], without accounting for vdw interaction. Because the studied compounds have vdw interaction, we found the system to have zero bandgap when using only GGA functionals with vdw interaction. This can be attributed to GGA functionals' usual flaw of underestimating band gaps when modelling strong exchange-correlations and relativistic effects, which prompted us to use the HSE06 functional to obtain

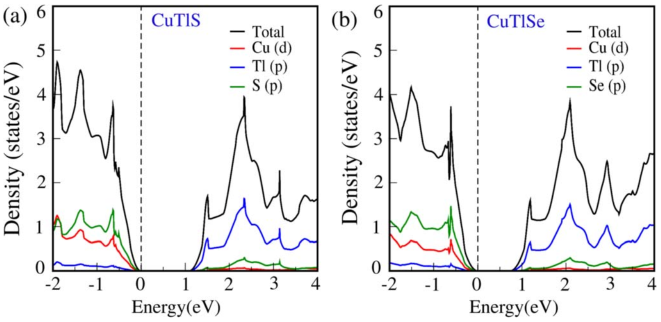

Figure 7. Density of states(a) CuTlS, (b) CuTlSe.

the correct electronic band gap. CuTlS and CuTlSe exhibit indirect band gaps of 1.01eV and 0.68 eV, respectively. These computed values are comparable to the bandgap values of Cu_2S (0.9 to 0.95 eV), Cu_2Se (0.8 eV), and SnSe (0.89 eV) [47–50]. A comparatively flat band edge along the $\Gamma - Z$ path suggests a significant thermoelectric characteristics along the 'c' direction. The Cu-*d* and S/Se-*p* orbitals dominate the valence bands at the Fermi level, whereas the Tl-*p* orbitals dominate the conduction bands, as evidenced by the total density of states and partial density of states plot (figure 7).

We used the AMSET code to analyze various scattering modes, responsible for acoustic and optical phonon-electron interactions in order to intuit the absolute value of transport parameters. Deformation potential, impurities, and atom displacement are the three main sources of scattering. Acoustic phonon-electron interaction is caused by the deformation potential, which results in a low-temperature phenomenon known as acoustic deformation potential scattering (ADP). When impurities scatter electrons in a system, this is known as impurity scattering (IMP). In high-temperature regimes, polar optical phonon scattering (POP) is dominated by atom displacement and contributed by optical phonon modes. Acoustic phonon branches contribute to state-independent elastic scattering. State-dependent inelastic scattering, on the other hand, is absolutely dominated by optical phonon branches. These scattering rates are used to compute relaxation time, which are then be used to compute various transport coefficients. Momentum relaxation time approximation (MRTA) is used to address elastic scattering processes, which are governed by the Fermi-Golden Rule.

$$\tau_{n\mathbf{k}\to m\mathbf{k}+\mathbf{q}}^{-1} = \frac{2\pi}{\hbar}|g_{nm}(\mathbf{k},\ \mathbf{q})|^2\delta(\Delta\varepsilon_{\mathbf{k},\mathbf{q}}^{nm}) \tag{1}$$

In the Inelastic process, scattering originates via phonon emission or absorption, which is expressed by a similar type of equation under Self-energy relaxation time approximation (SERTA),

$$\tau_{n\mathbf{k}\to m\mathbf{k}+\mathbf{q}}{}^{-1} = \frac{2\pi}{\hbar}|g_{nm}(k,\ q)|^2 \times \delta[(n_q+1-f_{mk+q}^0)$$
$$\delta(\Delta\epsilon_{k,q}^{nm} - \ \hbar\omega_q) + (n_q + f_{mk+q}^0)\delta(\Delta\epsilon_{k,q}^{nm} + \ \hbar\omega_q) \tag{2}$$

where, $-\hbar\omega_{\mathbf{q}}$ and $+\hbar\omega_{\mathbf{q}}$ correspond to scattering by emission and absorption of a phonon, respectively. At a constant temperature, IMP varies with concentration whereas ADP and POP remain fixed. The relaxation time is calculated by taking the reciprocal of the sum of individual scattering processes which is shown in figure 8.

3.3. Thermoelectric properties

The extremely dispersive electronic band structure and low lattice thermal conductivity further motivate us to investigate the thermoelectric characteristics at 300 K. The semiclassical Boltzmann transport theory is used in the next section to methodically analyse these electronic transport coefficients of CuTlX.

The Seebeck coefficient (S), electrical conductivity (σ), and electronic thermal conductivity (κ_e) are crucial parameters for assessing the electronic transport characteristics of thermoelectric materials. Figures 9(a), (b) shows the variation of thermopower with reference to varying carrier concentrations for holes and electrons, respectively. At higher concentrations, the thermopower values decline dramatically. Although the thermopower of both carriers is nearly identical, there is a little anisotropy in holes due to variations in band dispersion around the Fermi level along both the 'a' and 'c' axes. In the valence band region, the bands are essentially flat along the 'c' direction and dispersive along the 'a' direction, resulting in the anisotropic character of holes. In both the compounds, the electrical conductivity is of the order of 10^3 Sm^{-1}. Holes have a more prominent anisotropic character due to variations in dispersion in the valence band. The thermopower decreases as carrier concentration increases, whereas electrical conductivity has a cumulative effect. The electronic part of thermal conductivity is shown in figure 10. For both the compounds the κ_e is higher with p-type doping than n-type doping.

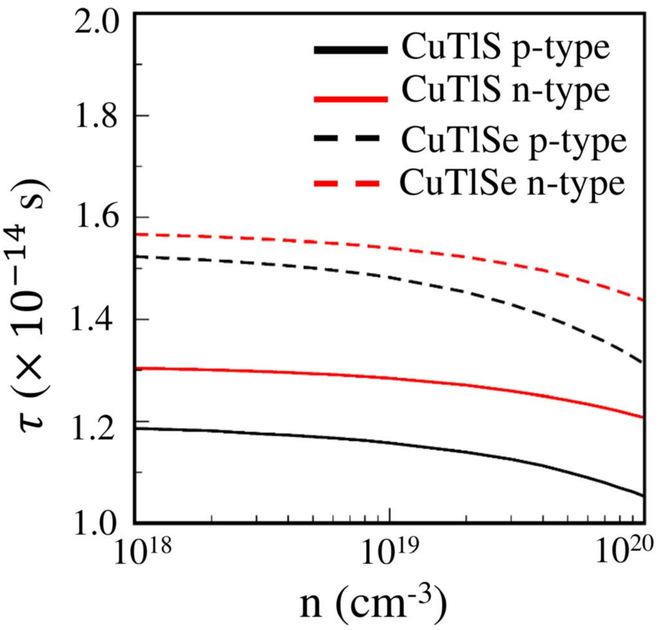

Figure 8. Variation of relaxation time with respect to concentration of carriers at 300 K.

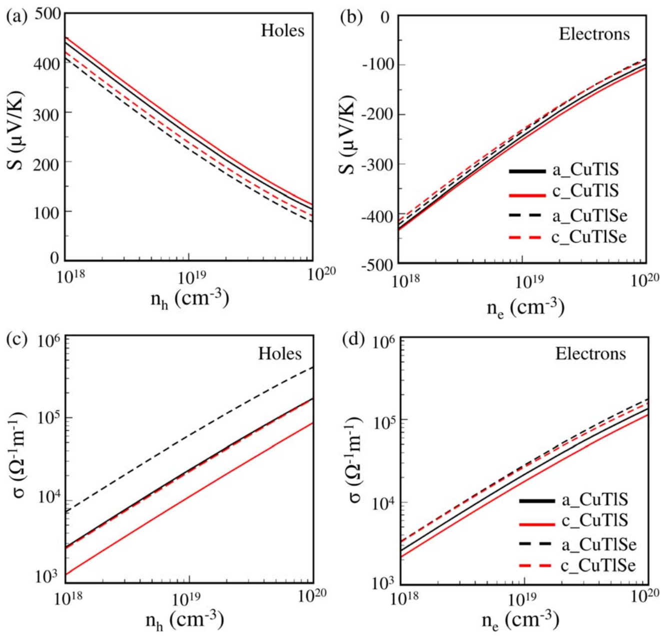

Figure 9. The thermoelectric coefficients of CuTlX, (a), (b) Seebeck coefficient(S) and (c), (d) electrical conductivity (σ) for holes and electrons respectively at 300 K.

The power factor is shown in figures 11(a) and (b). In power factor plots, the combined anisotropic influence of both thermopower and electrical conductivity is depicted. In both compounds, holes have a greater power factor than electrons, especially in the 'c' direction. Furthermore, p-type carriers have more anisotropy in the 'a' and 'c' directions than n-type carriers, thus their power factor is higher. We observed that, while both compounds' Seebeck coefficients decreased in similar manner, the large increase in conductivity aided in boosting the power factor of p-type CuTlSe. We have also calculated the compound's figure of merit to estimate its thermoelectric efficiency (figures 10(c), (d)). The low κ_l plays a critical role in the increase in ZT value of both holes and electrons in 'c' direction. The computed ZT values at 300 K for 10^{19} cm^{-3} concentration is given in table 3. These computed values are comparable with other Cu based compounds [18].

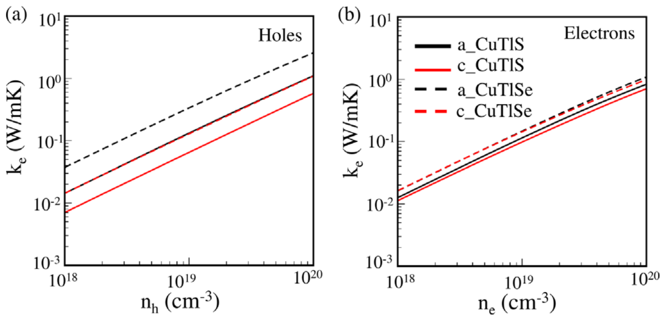

Figure 10. Electronic thermal conductivity of CuTlX (a), (b) for holes and electrons respectively at 300 K.

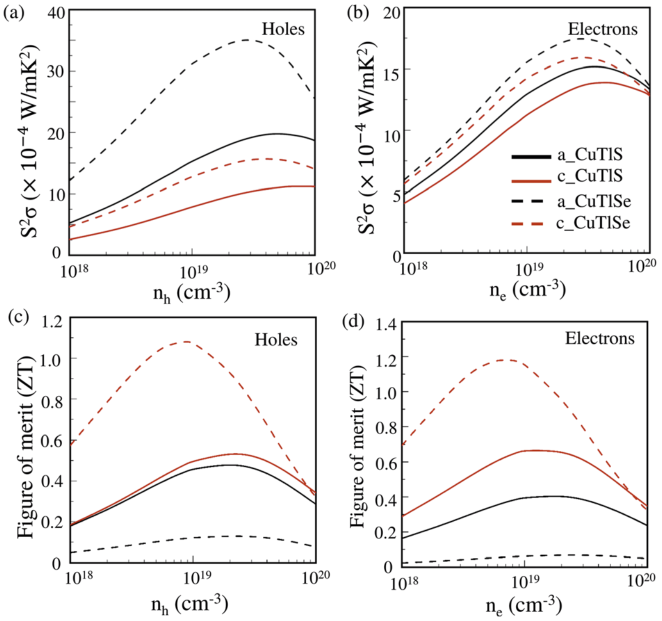

Figure 11. Power factor (a), (b) and thermoelec- tric figure of merit (c), (d) of CuTlX at T = 300 K for both holes and electrons respectively.

Table 3. *ZT* values of CuTlX at 300 K and 10^{19} cm^{-3}.

	Holes		Electrons	
	'a' direction	'c' direction	'a' direction	'c' direction
CuTlS	0.46	0.5	0.4	0.67
CuTlSe	0.12	1.08	0.06	1.16

3.4. Monolayer studies

CuTlX has a layered structure that enables it to cleave into a monolayer system due to the existence of vdw interaction. In order to avoid interactions with periodic images for the monolayer system, a vacuum with a thickness of 12 $\mathring{A}$ is created on both sides along the 'c' direction. To verify dynamical stability, phonon computations were performed along the high symmetry axes $\Gamma - X - M - \Gamma$ for monolayer [figure 12]. The stability is confirmed by the absence of imaginary phonon frequencies. To acquire a better understanding of the electronic structure, we used the HSE06 functional to compute the electronic band structure. Figure 13 shows the calculated band structure of monolayer CuTlX along the selected high-symmetry positions. CuTlS and CuTlSe monolayers are both semiconductors, with indirect band gaps of 2.02 eV and 1.74 eV, respectively. The increase in bandgap value of monolayers relative to bulk is due to the quantum confinement effect, which happens as a result of dimensional reduction.

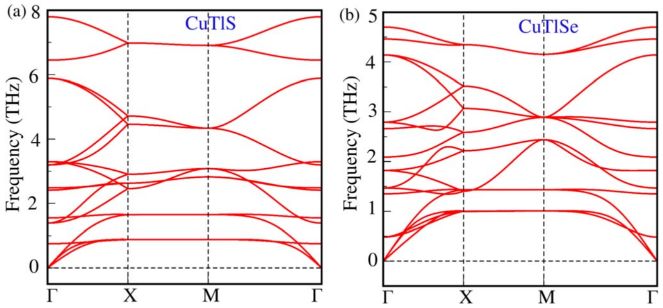

Figure 12. Phonon dispersion curves for monolayer (a) CuTlS (b) CuTlSe.

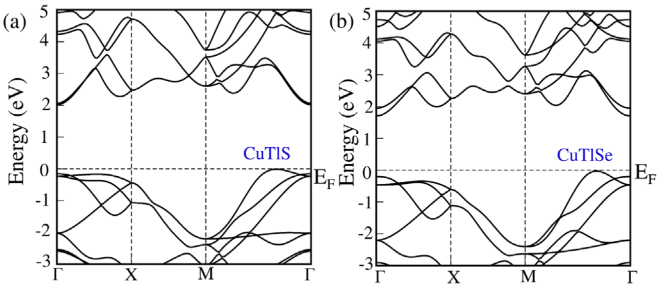

Figure 13. Electronic band structure of monolayer (a) CuTlS (b) CuTlSe.

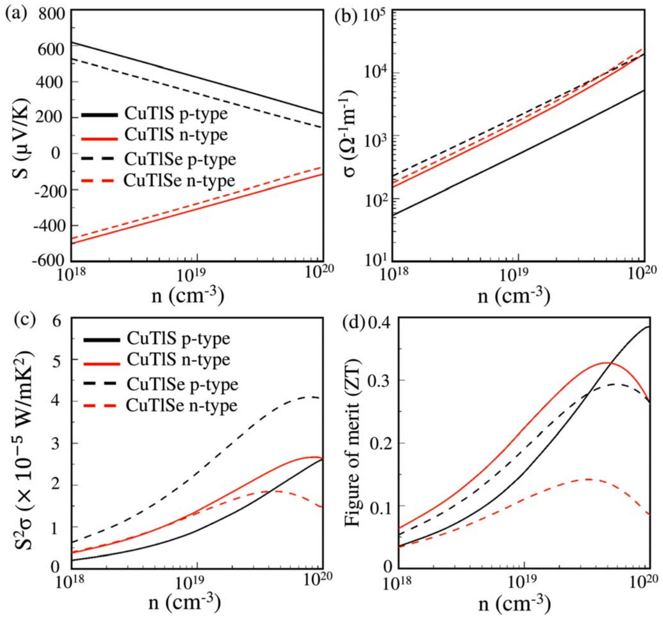

Figure 14. Calculated (a) Seebeck coefficients (b) Electrical conductivity (c) Power factor (d) *ZT* values for monolayers at 300 K.

We estimated the κ_l in the 'a' direction for monolayers as well. The κ_l in bulk forms is bigger than the layers in the 'a' direction, which is consistent with the notion that phonon thermal conductivity may be effectively reduced by reducing dimensionality. When compared to the CuTlSe monolayer, which has a κ_l of 0.351 W mK^{-1} at 300 K, the bulk monolayer of CuTlS has a low κ_l of 0.176 W mK^{-1}.

Similar to bulk, we have also studied the electronic transport properties in the monolayers at 300 K using AMSET code. The thermoelectric properties plotted as a function of carrier concentration at 300 K as shown in Figure 14. Thermopower for holes slightly higher than electrons at 300 K. Monolayers have a higher thermopower than the bulk at a carrier concentration of 10^{19} cm^{-3}. In CuTlS, the thermopower of holes and

Table 4. Maximum *ZT* values of CuTlX monolayer at 300 K.

Compounds	Holes	Concentration	Electrons	Concentration
CuTlS	0.39	1×10^{20} cm^{-3}	0.33	5×10^{19} cm^{-3}
CuTlSe	0.29	5×10^{19} cm^{-3}	0.14	4×10^{19} cm^{-3}

electrons increased from 254 μV/K to 424 μV/K, 243 μV/K to 307 μV/K, respectively, whereas in CuTlSe, the thermopower of holes and electrons increased from 225 μV/K to 334 μV/K, 235 μV/K to 277 μV/K, respectively. The electrical conductivity of both monolayers is of the order of $10^2 Sm^{-1}$, resulting in a decline in power factor despite an increase in seebeck coefficients. Due to the presence of quantum confinement in the examined compounds, the electrical conductivity of the monolayer is lower than that of the bulk. The low power factor is observed in both the compounds when compared with bulk. The carrier concentration range of $10^{19} - 10^{20}$ cm^{-3} is ideal for viable TE applications for monolayers. The maximal *ZT* values for CuTlS and CuTlSe monolayers for p-type and n-type doping are tabulated in table 4. From the computed values, it can be inferred that both doping methods would provide better results.

4. Conclusion

In conclusion, using state-of-the-art first-principles calculations, we explored the bulk and monolayer of CuTlX, a layered semiconductor, which exemplifies remarkable thermoelectric performance. The low lattice thermal conductivity, which is driven by low group velocity and low phonon lifetime, is the source of this high thermoelectric efficiency. CuTlSe has a high *ZT* value of 1.08 and 1.16 for holes and electrons in the out-of-plane 'c' direction at 300 K, indicating that these compounds have good thermoelectric properties. We also discovered an intriguing topological feature in CuTlS phonon band dispersion, confirming the existence of a nodal ring in the $\Gamma - X$ plane with nontrivial topological features, as well as a nonzero Berry phase value, indicating low lattice thermal conductivity in the 'a' direction. We performed a monolayer investigation of these compounds due to the presence of vdw interaction. The monolayers are likewise semiconducting in nature, with low lattice thermal conductivity, resulting in strong thermoelectric performance at 300 K for both carriers. Our findings offer information on CuTlX's fundamental phonon and electron transport characteristics, as well as its potential for thermoelectric applications.

Acknowledgments

Both Sushree Sarita Sahoo and V Kanchana would like to acknowledge CSIR project with sanction No.(03 (1433)/18/EMR-II) for financial support and IIT Hyderabad for providing computational facilities.

Data availability statement

The data that support the findings of this study are available upon reasonable request from the authors.

ORCID iDs

V Kanchana https://orcid.org/0000-0003-1575-9936

References

[1] Stern P C, Sovacool B K and Dietz T 2016 *Nat. Clim. Change* **6** 547–55
[2] Ovik R, Long B D, Barma M C, Riaz M, Sabri M F M, Said S M and Saidur R 2016 *Renew. Sustain. Energy Rev.* **64** 635–59
[3] Xiao Y and Zhao L-D 2020 *Science* **367** 1196–7
[4] Beretta D *et al* 2019 *Materials Science and Engineering: R: Reports* **138** 100501
[5] Ravichandran J *et al* 2014 *Nat. Mater.* **13** 168–72
[6] Shi X, Yang J, Salvador J R, Chi M, Cho J Y, Wang H, Bai S, Yang J, Zhang W and Chen L 2011 JACS **133** 7837–46
[7] Kleinke H 2010 *Chem. Mater.* **22** 604–11
[8] Maldovan M 2013 *Nature* **503** 209–17
[9] Xu Y, Gan Z and Zhang S-C 2014 *Phys. Rev. Lett.* **112** 226801
[10] Ouyang Y, Zhang Z, Li D, Chen J and Zhang G 2019 *Ann. Phys.* **531** 1800437
[11] Fu T, Yue X, Wu H, Fu C, Zhu T, Liu X, Hu L, Ying P, He J and Zhao X 2016 *Journal of Materiomics* **2** 141–9
[12] Zhao L-D *et al* 2013 JACS **135** 7364–70

[13] Wang H, Pei Y, LaLonde A D and Snyder G J 2012 *Proc. Natl Acad. Sci.* **109** 9705–9
[14] Kim S I *et al* 2015 *Science* **348** 109–14
[15] Rogl G, Grytsiv A, Rogl P, Peranio N, Bauer E, Zehetbauer M and Eibl O 2014 *Acta Mater.* **63** 30–43
[16] Liu H, Shi X, Xu F, Zhang L, Zhang W, Chen L, Li Q, Uher C, Day T and Snyder G J 2012 *Nat. Mater.* **11** 422–5
[17] Ge Z-H, Zhang B-P, Chen Y-X, Yu Z-X, Liu Y and Li J-F 2011 *Chem. Commun.* **47** 12697–9
[18] He Y, Day T, Zhang T, Liu H, Shi X, Chen L and Snyder G J 2014 *Adv. Mater.* **26** 3974–8
[19] Liu H *et al* 2013 *Adv. Mater.* **25** 6607–12
[20] Aliev Z S, Zúñiga F J, Koroteev Y M, Breczewski T, Babanly N B, Amiraslanov I R, Politano A, Madariaga G, Babanly M B and Chulkov E V 2016 *J. Solid State Chem.* **242** 1–7
[21] Tapp J H, Tang Z, Lv B, Sasmal K, Lorenz B, Chu P C W and Guloy A M 2008 *Phys. Rev.* B **78** 060505
[22] Kresse G and Hafner J 1993 *Phys. Rev.* B **47** 558
[23] Kresse G and Furthmüller J 1996 *Comput. Mater. Sci.* **6** 15–50
[24] Kresse G and Furthmüller J 1996 *Phys. Rev.* B **54** 11169
[25] Blöchl P E, Jepsen O and Andersen O K 1994 *Phys. Rev.* B **49** 16223
[26] Perdew J P, Burke K and Ernzerhof M 1996 *Phys. Rev. Lett.* **77** 3865
[27] Grimme S, Antony J, Ehrlich S and Krieg H 2010 *J. Chem. Phys.* **132** 154104
[28] Monkhorst H J and Pack J D 1976 *Phys. Rev.* B **13** 5188
[29] Heyd J, Scuseria G E and Ernzerhof M 2003 *J. Chem. Phys.* **118** 8207–15
[30] Togo A and Tanaka I 2015 *Scr. Mater.* **108** 1–5
[31] Gonze X and Lee C 1997 *Phys. Rev.* B **55** 10355
[32] Wu Q S, Zhang S N, Song H-F, Troyer M and Soluyanov A A 2018 *Comput. Phys. Commun.* **224** 405–16
[33] Togo A, Chaput L and Tanaka I 2015 *Phys. Rev.* B **91** 094306
[34] Ganose A M *et al* 2021 *Nat Commun* **12** 2222
[35] Ateser E, Ozisik H, Colakoglu K and Deligoz E 2011 *Comput. Mater. Sci.* **50** 3208–12
[36] Le P Y and Saxe P 2002 *Phys. Rev.* B **65** 104104
[37] Born M, Huang K and Lax M 1955 *Am. J. Phys.* **23** 474–474
[38] Wille F and Die Mathematik im Verlag B G T 1986 *Wechselwirkungen: Der Wissenschaftliche Verlag Als Mittler 175 Jahre B.G. Teubner 1811-1986, Vieweg+Teubner* (Wiesbaden: Verlag) pp 27–72
[39] Reuß A 1929 *ZAMM-Journal of Applied Mathematics and Mechanics/Zeitschrift für Angewandte Mathematik und Mechanik* **9** 49–58
[40] Hill R 1952 *Proceedings of the Physical Society. Section* A **65** 349
[41] Frantsevich I N 1982 Elastic constants and elastic moduli of metals and insulators. Reference book
[42] Belomestnykh V N and Tesleva E P 2004 *Tech. Phys.* **49** 1098–100
[43] Slack G A 1973 *J. Phys. Chem. Solids* **34** 321–35
[44] Fine M E, Brown L D and Marcus H L 1984 *Scr. Metall.* **18** 951–6
[45] Chan Y-H, Chiu C-K, Chou M Y and Schnyder A P 2016 *Phys. Rev.* B **93** 205132
[46] Singh S, Wu Q S, Yue C, Romero A H and Soluyanov A A 2018 *Physical Review Materials* **2** 114204
[47] Nam H N, Suzuki K, Nguyen T Q, Masago A, Shinya H, Fukushima T and Sato K 2022 *Phys. Rev.* B **105** 075205
[48] Liu W-D, Yang L and Chen Z-G 2020 *Nano Today* **35** 100938
[49] Choi J-H and Han Y-K 2015 *Curr. Appl Phys.* **15** 1417–20
[50] Soliman H S, Abdel Hady D A, Abdel Rahman K F, Youssef S B and El-Shazly A A 1995 *Physica A* **216** 77–84